

# Measurement of the $^1S_0$ neutron-neutron effective range in neutron-deuteron breakup

R. C. Malone,\* A. S. Crowell, L. C. Cumberbatch, B. A. Fallin,  
F. Q. L. Friesen, C. R. Howell, C. R. Malone, D. R. Ticehurst, and W. Tornow  
*Department of Physics, Duke University and Triangle Universities Nuclear Laboratory, Durham, NC*

D. M. Markoff and B. J. Crowe  
*Department of Mathematics and Physics, North Carolina Central University,  
and Triangle Universities Nuclear Laboratory, Durham, NC*

H. Witała  
*M. Smoluchowski Institute of Physics, Jagiellonian University, Kraków, Poland*  
(Dated: March 8, 2022)

We report the most precise determination of the neutron-neutron effective range parameter ( $r_{nn}$ ) from neutron-neutron quasifree scattering in neutron-deuteron breakup. The experiment setup utilized a collimated beam of 15.5 MeV neutrons and an array of eight neutron detectors positioned at angles sensitive to several quasifree scattering kinematic configurations. The two neutrons emitted from the breakup reaction were detected in coincidence and time-of-flight techniques were used to determine their energies. The beam-target luminosity was measured in-situ with the yields from neutron-deuteron elastic scattering. The value of  $r_{nn}$  was determined by comparing our cross-section data to rigorous Faddeev-type calculations using the CD Bonn nucleon-nucleon potential. We obtained a value of  $r_{nn} = 2.86 \pm 0.01$  (*stat*)  $\pm 0.10$  (*sys*) fm. This result was confirmed using a semilocal momentum-space regularized  $N^4\text{LO}^+$  chiral interaction potential.

Since the discovery of the neutron [1], much effort has been devoted to characterizing the properties of nuclei based on the interactions of their constituent nucleons. Due to the technical challenges associated with quantum chromodynamics, interactions between individual nucleons are described by effective theories [2]. Modern nucleon-nucleon ( $NN$ ) phenomenological potential models [3, 4], one-boson exchange models [5], and chiral effective theory [2, 6, 7] are used to describe  $NN$  scattering data. Because no direct neutron-neutron ( $nn$ ) scattering data exists, the isovector component of potential models are fit to proton-proton ( $pp$ ) scattering data. Neutron-neutron potentials are assumed to be the same as those for nuclear  $pp$  interactions due to charge symmetry [8] with small adjustments for charge-symmetry breaking effects such as the different masses of the neutron and proton [3, 9].

The  $^1S_0$   $nn$  scattering length ( $a_{nn}$ ) and effective range ( $r_{nn}$ ) have long been used to quantify charge-symmetry breaking in the  $NN$  interaction [10–12]. While there have been several recent measurements of  $a_{nn}$  to resolve a long-standing discrepancy [13–15], measurements of  $r_{nn}$  have not been published for over 40 years. Early experiments determined  $r_{nn}$  from the  $nn$  final state interaction (FSI) in various scattering systems but had large uncertainties and were not consistent [16–19]. Gabioud *et al.* extracted both  $a_{nn}$  and  $r_{nn}$  based on measurements of the photon energy spectrum from the reaction  $^2H(\pi^-, \gamma)2n$  and achieved the most precise result to date,  $r_{nn} = 2.80 \pm 0.11$  (*exp*)  $\pm 0.11$  (*theory*), consistent with charge symmetry [20–22]. More recently,  $r_{nn}$  was calculated from the value of  $a_{nn}$  determined from mea-

surements of  $nn$  FSI in neutron-deuteron ( $nd$ ) breakup [23, 24]. These determinations are not ideal because the low relative momentum between the neutrons in the  $nn$  FSI make this configuration much more sensitive to  $a_{nn}$  than to  $r_{nn}$ .

Neutron-neutron quasifree scattering (QFS) in the  $nd$  system is ideal for measuring  $r_{nn}$ . In this kinematic configuration, the momentum of the incident neutron is transferred exclusively to the neutron in the deuteron, i.e., the proton remains at rest in the laboratory frame during the scattering process. The cross section for  $nn$  QFS in  $nd$  breakup is highly sensitive to  $r_{nn}$  and is insensitive to off-shell effects of the  $NN$  potential, three-nucleon forces, and  $a_{nn}$  [25, 26]. For this reason, several early experiments determined  $r_{nn}$  from measurements of  $nn$  QFS in  $nd$  breakup. These experiments were performed at incident neutron energies between 14 and 25 MeV [27–31]. Although these measurements agreed well with theory, they were limited by large statistical uncertainties and were compared to theory which implemented several simplifying assumptions and used phenomenological  $NN$  interactions. A weighted average of the results gives a value of  $r_{nn} = 2.68 \pm 0.16$  fm, consistent with the value from Gabioud [10]. The recommended value of  $r_{nn} = 2.75 \pm 0.11$  fm is a weighted average of the  $\pi^-d$  and  $nn$  QFS measurements [10–12]. The average value is consistent with the charge-symmetric proton-proton value of  $r_{pp} = 2.85 \pm 0.04$  fm [10–12].

The situation was complicated by three recent measurements of  $nn$  QFS in  $nd$  breakup at incident neutron energies of 10.3, 26, and 25 MeV [32–34]. Rigorous Faddeev calculations [35] using the CD Bonn potential [5]

underpredicted the measured cross section by about 16% [26, 33, 34]; the theory predicted the shape of the data but not its magnitude. Inclusion of three-nucleon ( $3N$ ) forces did not significantly change the predicted cross section [25]. Experimentally, a large error ( $\approx 16\%$ ) in the determination of the beam-target luminosity would explain the discrepancy. On the theory side, the discrepancy could be removed by scaling the  $^1S_0$   $nn$  interaction matrix element by a factor of 1.08 [26]. However, this remedy drastically alters the value of  $r_{nn}$ , resulting in a significant charge-symmetry breaking effect [26].

We have performed new measurements of the cross section for  $nn$  QFS in  $nd$  breakup to investigate the discrepancy reported in Refs. [32–34]. In contrast to previous experiments, the integrated beam-target luminosity was determined from the yields for  $nd$  elastic scattering. This removes several sources of systematic uncertainty because the  $nd$  elastic scattering yields are measured simultaneously with the breakup yields and the absolute neutron flux and number of deuterium nuclei in the target do not need to be known independently. This technique has been successfully implemented in a previous measurement [36]. The present experiment was conducted at a different energy with more configurations sensitive to  $nn$  QFS than previous work [33, 34]. In this letter, we discuss the setup of the experiment, the data-analysis procedures, and the results for the kinematic configurations sensitive to  $r_{nn}$ . More details about the experiment and results from other  $nd$  breakup configurations will be discussed in a forthcoming publication.

Measurements were performed at the tandem accelerator facility at the Triangle Universities Nuclear Laboratory. The experiment setup is shown in Fig. 1. A beam of deuterons was directed into a 7.26-cm long cell of deuterium gas pressurized to 7.1 atm to produce neutrons at  $15.5 \pm 0.25$  MeV (full width) via the  $^2\text{H}(d, n)^3\text{He}$  reaction. The incident deuteron beam was pulsed ( $T = 400$  ns,  $\Delta t = 2$  ns FWHM) and the arrival of each beam pulse was detected by a capacitive beam pickoff unit immediately upstream of the deuterium gas cell. This provided a time reference for neutron time-of-flight (TOF) measurements. The average deuteron beam current on target was kept at 800 nA.

A copper collimator surrounded by a large shielding wall collimated the neutrons into a rectangular beam with a plateau of constant flux 36 mm wide  $\times$  55 mm high at the location of the  $\text{CD}_2$  target, which was suspended 177.6 cm downstream from the center of the neutron production cell.

Eight BC-501A liquid organic scintillators were used for neutron detection. The detectors were right cylinders (diameter = 12.7 cm, thickness = 5.08 cm) oriented with symmetry axes pointing at the scattering sample. Detectors were placed approximately 80 cm from the scattering sample (center-to-center distance) at nominal angles of  $10^\circ$ ,  $26^\circ$ ,  $40^\circ$ , and  $54^\circ$  on opposite sides of the neutron

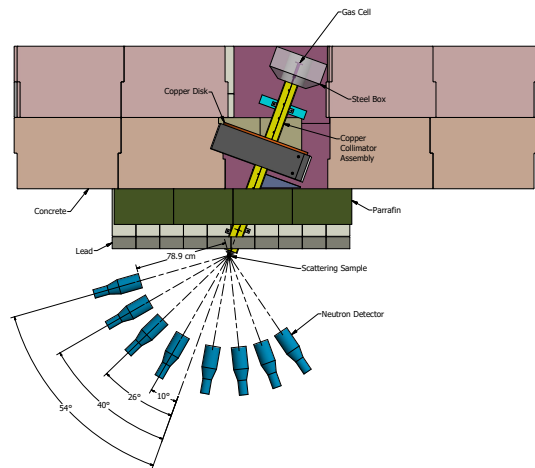


FIG. 1. A diagram of the experiment setup (distances are to scale). The  $\text{CD}_2$  sample is 177.6 cm from the center of the neutron production cell, and the detectors are located 80 cm from the target at nominal angles of  $10^\circ$ ,  $26^\circ$ ,  $40^\circ$ , and  $54^\circ$  on either side of the beam axis. More details are given in the text.

beam axis. The exact positions and scattering angles for each detector were determined from a survey of the detectors and scans of the neutron beam profile. Another cylindrical BC-501A scintillator (diameter = 3.81 cm, thickness = 3.81 cm) was placed in the neutron beam 507.4 cm downstream from the neutron production cell to monitor the neutron beam flux during data collection (not shown in Fig. 1).

To reduce background events, two cuts were applied to the data. A pulse-height threshold equal to one-half the energy of the  $^{137}\text{Cs}$  Compton-scattering edge (239 keV-electron-equivalent) was applied to the data to reduce backgrounds from low-energy particles. Pulse-shape discrimination techniques were used to reduce backgrounds from gamma-ray events.

Two right cylinders composed of deuterated polyethylene ( $\text{CD}_2$ , Cambridge Isotope Laboratories, Inc., DLM-220-0) and graphite were used as scattering samples. Physical properties of the samples are given in Table I. Each sample was mounted in the beam with their symmetry axes vertical. The entire volume of each sample was within the area of constant neutron flux. The graphite sample was used to measure backgrounds from neutrons scattering on carbon in the  $\text{CD}_2$  sample. Other backgrounds such as neutron scattering from air were measured with an empty sample holder.

To avoid unacceptably high dead times of the data acquisition system (DAQ), a trigger circuit with separate branches for single detector events and coincidence events was used. Coincidences between detectors on opposite sides of the neutron beam ( $\Delta\phi = 180^\circ$ ) within a window of 850 ns triggered the DAQ. The single-event

TABLE I. Properties of the scattering samples used.

Sample	Mass (g)	Diameter (mm)	Height (mm)
CD <sub>2</sub>	25.172	28.3	36.4
Graphite	42.055	28.6	38.0

branch trigger rate was divided by a factor of 10, delayed 400 ns, and vetoed by the coincidence branch before triggering the DAQ. This allowed all coincidence events to be measured with a reasonable DAQ dead time ( $\sim 10\%$ ) while accumulating sufficient counts from  $nd$  elastic scattering to achieve a statistical accuracy better than 0.1% in the beam-target luminosity determination.

Two types of coincidence TOF spectra were measured: (1) the raw coincidence spectrum containing true and accidental coincidences, and (2) the accidental coincidence spectrum. The accidental coincidence spectrum was measured by forming coincidences between events originating from two consecutive beam pulses ( $\Delta t \sim 400$  ns). An example is shown in Fig. 2.

A background due to detector cross talk, in which a single neutron scattered between two detectors and was detected in both, contributed to the raw coincidence spectrum. These events were separated by less than 100 ns in time and were indistinguishable from real  $nn$  coincidences. However, due to the experiment geometry, these events fell outside the TOF region of the data reported here. Coincidences due to cross talk form the diagonal bands indicated by the red trapezoids in the top panel of Fig. 2.

For each detector pair, the raw and accidental coincidence spectra were projected onto the ideal kinematic locus of allowed neutron energies, referred to as the  $S$  curve. The variable  $S$  measures the arc length along the curve in a counterclockwise direction beginning at the point where the energy of the second neutron reaches a minimum [35, 36]. The projection was carried out in the  $k_1 - k_2$  plane, where the momenta of the two breakup neutrons ( $k_1$  and  $k_2$ ) in each breakup event define a point in that plane. The  $S$  curve was divided into 0.5 MeV-wide bins. Each detected event was projected into the nearest bin on the  $S$  curve. We used the technique of Ref. [37], which produces equivalent results to the method used in a previous experiment [36, 38]. The projected accidental coincidence spectrum was subtracted from the projected raw spectrum for each detector pair.

The present data were compared to rigorous ab-initio three-body calculations using the CD-Bonn potential [5] and the semilocal momentum-space (SMS) regularized  $N^4LO^+$  chiral interaction of the Bochum group [7] with the cutoff  $\Lambda = 450$  MeV in the Faddeev formalism applying the technique described in Ref. [35]. A Monte-Carlo (MC) simulation of the experiment was used to average the point-geometry theory predictions over the energy spread and finite geometry of the experiment to

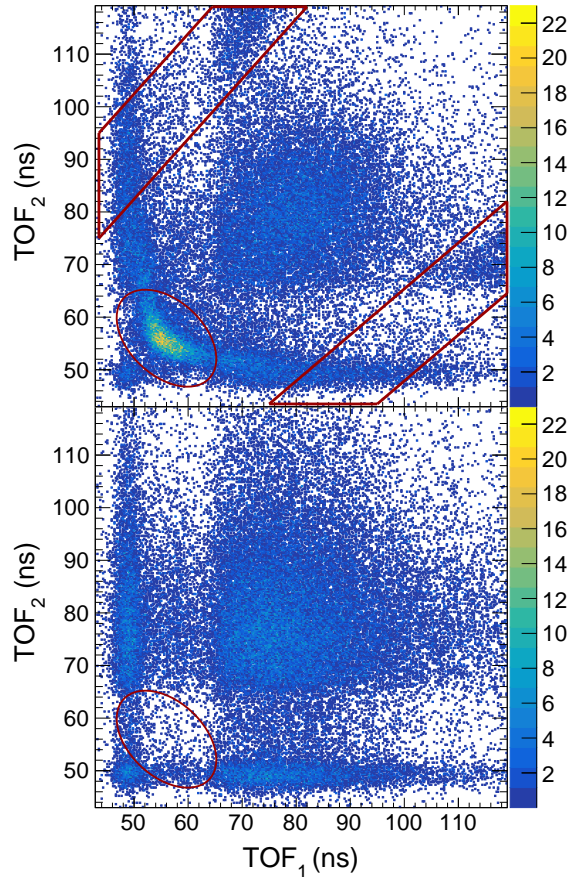


FIG. 2. Raw (top) and accidental (bottom) two-dimensional coincidence TOF spectra for the detectors at  $40^\circ$  on opposite sides of the beam axis. The  $nn$  QFS region is indicated by the red ellipse. Accidental coincidences from elastic and inelastic neutron scattering in the sample form the horizontal and vertical bands at  $\text{TOF} = 50$  ns. The large mound of accidental coincidences in the center is due to neutrons produced by deuteron breakup reactions in the gas cell ( $E_n < 10$  MeV) that scatter elastically from the sample. Regions affected by cross talk are enclosed in the red trapezoids. Cross-talk events are clearly visible as enhancements in the upper right corner of each trapezoid.

allow accurate comparison between theory and data. The MC simulation was also used to determine the average values of the product of neutron detector efficiencies and neutron transmission probabilities as a function of  $S$ . Finally, the simulation was used to quantify contributions of background processes to neutron scattering yields. The details of the simulation can be found in Ref. [36].

Background processes that were simulated for both breakup and  $nd$  elastic scattering included: multiple scattering of neutrons in the sample, in-scattering of neutrons from shielding materials and adjacent detectors, and neutrons produced via  ${}^2H(d,n){}^3He$  on deuterons implanted in the gold beam stop. Two additional backgrounds for

$nd$  elastic scattering were simulated: neutrons scattering from the 1.6% hydrogen impurity in the  $CD_2$  sample, and  $nd$  breakup events in which only one neutron was detected. The fraction of background events determined with the MC simulation was subtracted from the measured  $nn$  coincidence yields and the  $nd$  elastic scattering yields. The corrections for elastic scattering were between 7-12% and the average correction for breakup events varied from 6-8%, depending on the scattering configuration.

The yields from  $nd$  elastic scattering in each detector were used to determine the integrated beam-target luminosity. Backgrounds from neutrons scattering on carbon and air were measured using the graphite sample and an empty target holder. The TOF spectrum for each detector accumulated with the empty target holder were subtracted from the spectra measured with the  $CD_2$  and graphite samples. The TOF spectra measured with the empty target holder were normalized to the spectra measured with the  $CD_2$  and graphite samples using the integrated beam current (BCI), the gas pressure in the neutron production cell, and the DAQ live time fraction. The TOF spectra measured with the graphite sample were normalized to the spectra measured with the  $CD_2$  sample in a similar way. The normalization factor also included the ratio of carbon nuclei in the two samples determined using data from a previous experiment [36]. The normalized graphite TOF spectra were subtracted from the  $CD_2$  TOF spectra to obtain the raw yields from  $nd$  elastic scattering. Also, the raw yields were corrected for backgrounds quantified with the MC simulation.

The luminosity per BCI measured by all eight detectors agreed with a standard deviation of 2.1%. The geometric mean of the beam-target luminosity measured by all detectors except those at  $10^\circ$  was used to compute the breakup cross section. The  $nd$  yields measured by the detectors at  $10^\circ$  were excluded from the luminosity determination because of the large uncertainty in subtracting the background contributions ( $\sim 70\%$ ) due to neutron scattering on carbon and air.

Several  $nn$  QFS configurations were measured using detectors positioned on opposite sides of the beam axis. The detector pair at  $\theta_1 = \theta_2 = 40^\circ$  measured an exact quasifree scattering configuration. The detector pair at  $\theta_1 = \theta_2 = 26^\circ$  and the two pairs at  $\theta_1 = 26^\circ$ ,  $\theta_2 = 40^\circ$ , measured configurations near  $nn$  QFS, where the proton energy reaches a minimum of 0.4 MeV and 0.1 MeV, respectively. Two other  $nn$  QFS configurations were measured; however, the cross sections for those configurations are dominated by  $np$  final-state interactions and so they were not used to determine  $r_{nn}$ .

Our results for the  $nn$  QFS cross section are presented in Fig. 3. The measured data are given by the points and the error bars represent statistical uncertainty. The data points for the configuration at  $\theta_1 = 26^\circ$ ,  $\theta_2 = 40^\circ$  are a statistically weighted average of the results from the two

detector pairs. Not shown on the plot is a systematic uncertainty of  $\pm 6.3\%$ . The curves in Fig. 3 represent the result of the MC simulation using  $nd$  breakup cross sections calculated with the CD Bonn potential with different values of  $r_{nn}$ . The curves provide a representative sample covering the full range of the values  $r_{nn}$  used in the analysis.

TABLE II. Sources of systematic uncertainty in the determination of the cross section for  $nn$  QFS in  $nd$  breakup. All uncertainties are given as one standard deviation.

Source	Magnitude (%)
Coincidence yields	1.5
Elastic scattering yields	2.8
Efficiency normalization	2.9
Efficiency shape	3.0
Detector gain drift	1.0
Neutron transmission	2.7
$nd$ elastic cross section	1.6
Detector solid angle	0.9
Single event live time	0.1
Coincidence event live time	0.6
Total	6.3

Sources of systematic uncertainty are listed in Table II. The uncertainty in the measured  $nn$  coincidence yields is mainly due to the MC corrections for multiple scattering and in-scattering, but also includes contributions from the accidental background subtraction and neutrons produced at energies below 15.5 MeV via  $(d, n)$  reactions on contaminants in the gas cell. Subtraction of the graphite spectra and simulated backgrounds contribute the most to the uncertainty in the extracted elastic scattering yields. The MC simulation uses as input simulated detector efficiency curves fit to measurements of the neutron flux from the  ${}^2H(d, n){}^3He$  reaction at zero degrees [39, 40]. The uncertainty in the overall normalization and shape of the efficiency curve were determined from those measurements as in Ref. [36]. The effect of small changes in the detector gain on the simulated detector efficiency was estimated using variations of the efficiency curve due to changes in the detector threshold setting. Neutron transmission factors were calculated with the MC simulation using cross sections and associated uncertainties from ENDF/B-VII.1 [41]. The  $nd$  elastic scattering cross section was computed using the CD Bonn potential, and the error is estimated as the difference between predictions of several modern  $NN$  potentials [42]. The uncertainty in the detector solid angle is due to the precision of measuring the positions of the detector faces (0.1 cm). The difference between multiple methods used to determine the DAQ live time fraction is used as an estimate of the uncertainty.

To determine  $r_{nn}$ , the MC simulation was run using breakup cross sections calculated with the CD Bonn  $nn$   ${}^1S_0$  matrix element scaled by seven different factors, re-

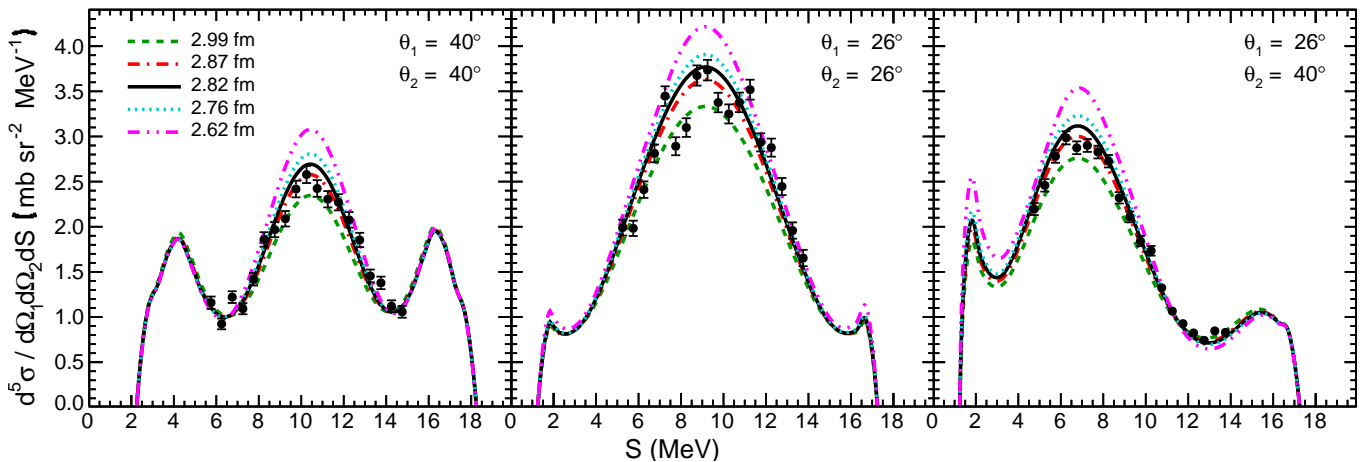


FIG. 3. Plot of the measured  $nd$  breakup cross section as a function of  $S$  for the  $nn$  QFS configurations most sensitive to  $r_{nn}$ . The error bars represent statistical uncertainties only; there is a systematic uncertainty of  $\pm 6.3\%$ . The solid curve is the result of the MC simulation using the standard CD Bonn potential. Other curves represent the MC simulation result using the CD Bonn potential with values of  $r_{nn}$  indicated by the legend in the top panel.

sulting in different values of  $r_{nn}$ . Scaling this matrix element also alters  $a_{nn}$ ; however, because the  $nn$  QFS cross section is sensitive only to variations in the effective range and not the scattering length, this is adequate to determine  $r_{nn}$  [26]. For every detector configuration, the value of  $\chi^2$  was computed as a function of  $r_{nn}$  using the integral of the cross section over the QFS peak where the sensitivity to changes of  $r_{nn}$  is greatest. A second-degree polynomial was fit to the  $\chi^2$  function and the minimum of this fit was taken as the best value of  $r_{nn}$ . The statistical uncertainty in the extracted value of  $r_{nn}$  is given by  $\Delta r_{nn} = |r_{nn}(\chi_{min}^2 + 1) - r_{nn}(\chi_{min}^2)|$ . The integral of the QFS theoretical cross section as a function of  $r_{nn}$  was used to convert the systematic uncertainty in the cross section to uncertainty in  $r_{nn}$ . The analysis was repeated using the SMS chiral  $N^4LO^+$  potential of the Bochum group [7] with the cutoff  $\Lambda = 450$  MeV. Our results are summarized in Table III. The values of  $r_{nn}$  determined from the three  $nn$  QFS configurations agreed within statistical uncertainties. The final result is given as a weighted average of those values. The values extracted using the two different potentials agree well, and our values are consistent with the recommended value  $r_{nn} = 2.75 \pm 0.11$  fm and the charge-symmetric value of  $r_{pp} = 2.85 \pm 0.04$  fm [10–12].

We have performed measurements of the cross section for  $nn$  QFS in  $nd$  breakup using a new technique to determine the integrated beam-target luminosity based on the  $nd$  elastic scattering yields measured simultaneously with the  $nn$  coincidences from  $nd$  breakup. Our results, summarized in Table III, provide the first measurement of the  $nn$  effective range parameter using modern  $NN$  potentials and the most precise determination from  $nn$  QFS in  $nd$  breakup. The data also suggest that the previously reported discrepancies between theory and data

TABLE III. Values of  $r_{nn}$  determined from different angular configurations in this experiment using the CD-Bonn potential. The last two rows give the weighted average determined using the CD Bonn and  $N^4LO^+$  potentials. See text for details.

Configuration	$r_{nn}$ (fm)
$\theta_1 = 40^\circ \theta_2 = 40^\circ$	$2.85 \pm 0.02$ (stat) $\pm 0.09$ (sys)
$\theta_1 = 26^\circ \theta_2 = 26^\circ$	$2.86 \pm 0.01$ (stat) $\pm 0.11$ (sys)
$\theta_1 = 26^\circ \theta_2 = 40^\circ$	$2.87 \pm 0.02$ (stat) $\pm 0.10$ (sys)
CD Bonn Average	$2.86 \pm 0.01$ (stat) $\pm 0.10$ (sys)
$N^4LO^+$ Average	$2.87 \pm 0.01$ (stat) $\pm 0.10$ (sys)

in the  $nn$  QFS cross section at 10.3, 26 and 25 MeV [32–34] are due to systematic errors in the determination of the beam-target luminosity leading to incorrect normalization of the breakup cross section. Also, it is possible that the discrepancy is strongly energy dependent and occurs at incident neutron energies above 16 MeV. Further measurements at higher incident neutron energies should be carried out to investigate this possibility.

The authors thank the TUNL technical staff for their contributions. The authors appreciate the use of the supercomputer cluster of the JSC in Jülich, Germany, where parts of the numerical calculations were performed. This work is supported in part by the U.S. Department of Energy under grant Nos. DE-FG02-97ER41033 and DE-SC0005367 and by the Polish National Science Center under grant No. DEC-2016/22/M/ST2/00173. This work was performed under the auspices of the U.S. Department of Energy by Lawrence Livermore National Laboratory under Contract DE-AC52-07NA27344.

- 
- \* Present address: Lawrence Livermore National Laboratory; malone18@llnl.gov
- [1] J. Chadwick, *Nature* **129**, 312 (1932); *Proc. R. Soc. London A* **136**, 692 (1932).
- [2] R. Machleidt and D. R. Entem, *Phys. Rep.* **503**, 1 (2011).
- [3] V. G. J. Stoks, R. A. M. Klomp, C. P. F. Terheggen, and J. J. de Swart, *Phys. Rev. C* **49**, 2950 (1994).
- [4] R. B. Wiringa, V. G. J. Stoks, and R. Schiavilla, *Phys. Rev. C* **51**, 38 (1995).
- [5] R. Machleidt, F. Sammarruca, and Y. Song, *Phys. Rev. C* **53**, R1483 (1996); R. Machleidt, **63**, 024001 (2001).
- [6] E. Epelbaum, H.-W. Hammer, and Ulf.-G. Meißner, *Rev. Mod. Phys.* **81**, 1773 (2009).
- [7] P. Reinert, H. Krebs, and E. Epelbaum, *Eur. Phys. J. A* **54**, 86 (2018).
- [8] W. Heisenberg, *Z. Phys.* **77**, 1 (1932).
- [9] V. G. J. Stoks, R. A. M. Klomp, M. C. M. Rentmeester, and J. J. de Swart, *Phys. Rev. C* **48**, 792 (1993).
- [10] I. Šlaus, Y. Akaishi, and H. Tanaka, *Phys. Rep.* **173**, 257 (1989).
- [11] G. A. Miller, B. M. K. Nefkens, and I. Šlaus, *Phys. Rep.* **194**, 1 (1990).
- [12] R. Machleidt and I. Šlaus, *J. Phys. G* **27**, R69 (2001).
- [13] C. R. Howell, Q. Chen, *et al.*, *Phys. Lett. B* **444**, 252 (1998); Q. Chen, C. R. Howell, *et al.*, *Phys. Rev. C* **77**, 054002 (2008).
- [14] D. E. González Trotter *et al.*, *Phys. Rev. Lett.* **83**, 3788 (1999); D. E. Gonzalez Trotter *et al.*, *Phys. Rev. C* **73**, 034001 (2006).
- [15] V. Huhn, L. Wätzold, Ch. Weber, A. Siepe, W. von Witsch, H. Witała, and W. Glöckle, *Phys. Rev. Lett.* **85**, 1190 (2000); *Phys. Rev. C* **63**, 014003 (2000).
- [16] E. Baumgartner, H. E. Conzett, E. Shield, and R. J. Slobodrian, *Phys. Rev. Lett.* **16**, 105 (1966).
- [17] E. E. Gross, E. V. Hungerford, J. J. Malanify, and R. Woods, *Phys. Rev. C* **1**, 1365 (1970).
- [18] B. Zeitnitz, R. Maschuw, P. Suhr, and W. Ebenhöf, *Phys. Rev. Lett.* **28**, 1656 (1972); B. Zeitnitz, R. Maschuw, P. Suhr, W. Ebenhöf, J. Bruinsma, and J. H. Stuivenberg, *Nucl. Phys. A* **231**, 13 (1974).
- [19] J. Kecskeméti, T. Czibók, and B. Zeitnitz, *Nucl. Phys. A* **254**, 110 (1975).
- [20] B. Gabioud *et al.*, *Phys. Rev. Lett.* **42**, 1508 (1979).
- [21] B. Gabioud *et al.*, *Phys. Lett. B* **103**, 9 (1981).
- [22] B. Gabioud *et al.*, *Nucl. Phys. A* **420**, 496 (1984).
- [23] V. A. Babenko and N. M. Petrov, *Phys. Atom. Nucl.* **76**, 684 (2012).
- [24] S. V. Zuyev, E. S. Konobeevski, M. V. Mordovskoy, and S. I. Potashev, *Bull. Rus. Acad. Sci. Phys.* **73**, 796 (2009); E. S. Konobeevski, Yu. M. Burmistrov, S. V. Zuyev, M. V. Mordovskoy, and S. I. Potashev, *Phys. Atom. Nucl.* **73**, 1302 (2010); E. S. Konobeevski, V. I. Kukulin, M. V. Mordovskoi, V. N. Pomerantsev, S. I. Potashev, O. A. Rubtsova, V. A. Sergeev, S. V. Zuev, and I. M. Sharapov, *Bull. Rus. Acad. Sci. Phys.* **75**, 443 (2011).
- [25] H. Witała and W. Glöckle, *J. Phys. G* **37**, 064003 (2010).
- [26] H. Witała and W. Glöckle, *Phys. Rev. C* **83**, 034004 (2011).
- [27] I. Šlaus, J. W. Sunier, G. Thompson, J. C. Young, J. W. Verba, D. J. Margaziotis, P. Doherty, and R. T. Cahill, *Phys. Rev. Lett.* **26**, 789 (1971).
- [28] E. Bovet, F. Foroughi, and J. Rossel, *Nucl. Phys. A* **304**, 29 (1978).
- [29] J. Soukup, J. M. Cameron, H. W. Fielding, A. H. Hussein, S. T. Lam, and G. C. Neilson, *Nucl. Phys. A* **322**, 109 (1979).
- [30] H. Guratzsch, B. Kühn, H. Kumpf, J. Mösner, W. Neubert, W. Pilz, G. Schmidt, and S. Tesch, *Nucl. Phys. A* **342**, 239 (1980).
- [31] W. von Witsch, B. Gómez Moreno, W. Rosenstock, R. Franke, and B. Steinheuer, *Phys. Lett. B* **91**, 342 (1980).
- [32] W. Lübcke, *Kinematisch vollständige Messungen an der Reaktion  $^2\text{H}(n,nn)^1\text{H}$  bei  $E_n = 10$  MeV in FSI-Konfigurationen*, Ph.D. thesis, University of Bochum (1992).
- [33] A. Siepe, J. Deng, V. Huhn, L. Wätzold, Ch. Weber, W. von Witsch, H. Witała, and W. Glöckle, *Phys. Rev. C* **65**, 034010 (2002).
- [34] X. C. Ruan *et al.*, *Phys. Rev. C* **75**, 057001 (2007).
- [35] W. Glöckle, H. Witała, D. Hüber, H. Kamada, and J. Golak, *Phys. Rep.* **274**, 107 (1996).
- [36] R. C. Malone *et al.*, *Phys. Rev. C* **101**, 034002 (2020).
- [37] W. Parol *et al.*, *Phys. Rev. C* **102**, 054002 (2020).
- [38] E. Finckh, K. Geissdörfer, R. Lin, S. Schindler, and J. Strate, *Nucl. Instr. Methods A* **262**, 441 (1987).
- [39] G. Dietze and H. Klein, *NRESP4 and NEFF4 Monte Carlo Codes for the Calculation of Neutron Response Functions and Detection Efficiencies for NE 213 Scintillation Detectors*, Tech. Rep. PTB-ND-22 (Physikalisch-Technische Bundesanstalt, Braunschweig, Germany, 1982).
- [40] M. Drosg and N. Otuka, *Evaluation of the Absolute Angle-Dependent Differential Neutron Production Cross Sections by the Reactions  $^3\text{H}(p,n)^3\text{He}$ ,  $^1\text{H}(t,n)^3\text{He}$ ,  $^2\text{H}(d,n)^3\text{He}$ ,  $^3\text{H}(d,n)^4\text{He}$ , and  $^2\text{H}(t,n)^4\text{He}$  and of the Cross Sections of Their Time-Reversed Counterparts up to 30 MeV and Beyond*, Tech. Rep. INDC(AUS)-0019 (IAEA Nuclear Data Section, Vienna, Austria, 2015).
- [41] M. B. Chadwick, M. Herman, P. Obložinský, *et al.*, *Nucl. Data Sheets* **112**, 2887 (2011), special Issue on ENDF/B-VII.1 Library.
- [42] R. Skibiński, Yu. Volkotrub, J. Golak, K. Topolnicki, and H. Witała, *Phys. Rev. C* **98**, 014001 (2018).